UK Atomic
Energy
Authority

UKAEA-CCFE-PR(21)76

S. Mijin, F. Militello, S. Newton, J.T. Omotani, R.J. Kingham

Kinetic and fluid simulations of parallel electron transport during equilibria and transients in the Scrape-Off Layer

Enquiries about copyright and reproduction should in the first instance be addressed to the UKAEA Publications Officer, Culham Science Centre, Building K1/0/83 Abingdon, Oxfordshire, OX14 3DB, UK. The United Kingdom Atomic Energy Authority is the copyright holder.

The contents of this document and all other UKAEA Preprints, Reports and Conference Papers are available to view online free at scientific-publications.ukaea.uk/

Kinetic and fluid simulations of parallel electron transport during equilibria and transients in the Scrape-Off Layer

S. Mijin, F. Militello, S. Newton, J.T. Omotani, R.J. Kingham

This is a preprint of a paper submitted for publication in
Plasma Physics and Controlled Fusion

Kinetic and fluid simulations of parallel electron transport during equilibria and transients in the Scrape-Off Layer

S. Mijin[1], **F. Militello**[2], **S. Newton**[2], **J. Omotani**[2], **and R. J. Kingham**[1]

[1]Blackett Lab., Plasma Physics Group, Imperial College, London SW7 2AZ, UK
[2]CCFE, Culham Science Centre, Abingdon, Oxon OX14 3DB, UK

E-mail: `stefan.mijin14@imperial.ac.uk`

September 2019

Abstract. We present the first parallel electron transport results obtained using the newly developed 1D transport code SOL-KiT. In order to properly predict divertor heat loads it is of key importance to develop a thorough understanding of discrepancies between different parallel transport modelling approaches. With the capability to self-consistently switch between a kinetic and a fluid model for the electrons, we explore and report the differences in both equilibrium and transient simulations. Equilibria are obtained for an input power scan with parameters relevant to medium size tokamaks. Simulations of input power perturbations have been performed using both electron models. Significant kinetic effects are found during transients, especially in the behaviour of the electron sheath heat transmission coeficient, which shows up to an almost tenfold increase. We discuss the implications of the presented results to potential modelling decisions, as well as possible extensions to the used model.

1. Introduction

The Scrape-Off Layer (SOL) is the edge region of Magnetically Confined Fusion (MCF) devices, through which the energy and particles which escape the fusion core travel to the plasma-facing components of the reactor. Transport occurs along and across the open field lines of the SOL, and understanding it is a key issue for future reactor design[1]. Parallel transport carries energy and particles from the hot upstream to the divertor targets, and determines, in combination with other physical processes (such as atomic and molecular physics), the divertor heat load. Fluid modeling is typically adopted when tackling the problem of parallel transport, utilizing the classical results of Braginskii[2], and allowing modification of the heat flux through the use of flux limiters[3]. However, as the parallel direction of the SOL is characterized by large gradients in both temperature and density (and thus collisionality), kinetic effects can modify transport properties, and have been proposed as potential causes of discrepancy between fluid simulations and experimental results[4].

Previous numerical studies of kinetic effects in the SOL have been perfomed with a wide array of codes, including both PIC[5, 6] and finite-difference codes[7, 8, 9, 10, 11, 12]. These studies report the impact of kinetic effects in various aspects of parallel transport, including the modification of the parallel heat flux and atomic rates[9], as well as effects on the properties of the plasma sheath. Havlickova et al.[13] compare the results of different fluid and kinetic codes during simulations of Edge-Localized Modes (ELMs), and report sensitivity of target heat flux peak values to applied flux limiters.

These existing studies mainly focused on very (machine-)specific scenarios, and general parameter scans are hard to find. This study is a first attempt at such an approach, tackling the comparison between a fluid and kinetic model of parallel electron transport, with a focus on fundamental discrepancies. We use the newly developed transport code SOL-KiT (Scrape-Off Layer Kinetic Transport)[14], where electrons can be treated as either a fluid or kinetically, while ions are treated as a fluid. SOL-KiT also includes a basic self-consistent treatment of atomic processes in a pure deuterium plasma.

We start by presenting the basics of the SOL-KiT model, before moving on to the first results. The input power has been scanned in both fluid and kinetic modelling, and the equilibrium results are reported and compared to examine kinetic effects in steady state. The parameters used are relevant to medum size tokamaks (MSTs), where a current research concern is the interaction of transients with detachment. Transients are launched on the simulated equilibria, and the resulting evolution of various quantities, including the temperature at the target, are presented, showing significant kinetic effects. We close by summarising the electron transport model used, noting its limitations and considered extensions, and discussing the results obtained in this study.

2. The SOL-KiT model

The SOL system of interest is represented as a straightened-out 1D SOL, with the x-axis being along the magnetic field line. The upstream point $x = 0$ is taken to be the symmetry plane, while the downstream boundary is at the entrance of the target sheath.

We solve equations for the electrons, ions, atomic neutrals, as well as the parallel electric field. For the electrons we can use either fluid or kinetic equations, both of which are self-consistently coupled to the rest of the model, treating the same physics using the same data, with only the level of detail varying. This allows for clean comparisons between the models, which are the focus of this study. The ions are a fluid, while neutrals obey a diffusive-reactive Collisional Radiative model.

2.1. Fluid and neutral equations

The three fluid electron equations are

$$\frac{\partial n_e}{\partial t} + \frac{\partial (n_e u_e)}{\partial x} = S, \tag{1}$$

$$\frac{\partial u_e}{\partial t} = -u_e\frac{\partial u_e}{\partial x} - \frac{e}{m_e}E + \frac{R_{ei}+R_{en}}{m_e n_e} - \frac{S}{n_e}u_e - \frac{1}{m_e n_e}\frac{\partial (n_e k T_e)}{\partial x}, \tag{2}$$

$$\frac{\partial kT_e}{\partial t} = -u_e\frac{\partial kT_e}{\partial x} + \frac{2}{3}\left[\frac{Q}{n_e} - kT_e\frac{\partial u_e}{\partial x} - \frac{1}{n_e}\frac{\partial q_e}{\partial x}\right] - \frac{2}{3}\left[\frac{S}{n_e}\left(\frac{3}{2}kT_e - \frac{m_e u_e^2}{2}\right) + \frac{u_e(R_{ei}+R_{en})}{n_e}\right], \tag{3}$$

where E is the electric field in the parallel direction and $S = S_{ion} + S_{rec}$ is the ionization and recombination particle source. n_e and T_e are the electron density and temperature, respectively, while u_e is the parallel flow velocity of the electron fluid. The friction $R_{ei} = R_T + R_u$ is taken from Braginskii[2] with $R_u = -m_e n_e 0.51(u_e - u_i)/\tau_e$ and $R_T = -0.71 n_e \partial(kT_e)/\partial x$, where the τ_e is the electron-ion collision time[2]. R_{en} is the total electron-neutral friction, calculated using a slowly drifting Maxwellian for the electrons.

The heat flux $q_e = q_T + q_u$ is given by $q_T = -\kappa_e \partial(kT_e)/\partial x$ and $q_u = 0.71 n_e kT_e(u_e - u_i)$, with $\kappa_e = 3.2 n_e kT_e \tau_e/m_e \propto T_e^{5/2}$ being the classical Spitzer-Härm value. The external heating in the temperature equation is given by Q.

For the ions (of charge Ze) we take both $Zn_i = n_e$, and assume $T_i = T_e$ (see Section 3 for more on the effect of this approximation). This leaves just the ion momentum equation

$$\frac{\partial u_i}{\partial t} = -u_i\frac{\partial u_i}{\partial x} + \frac{Ze}{m_i}E + \frac{R_{ie}+R_{CX}}{m_i n_i} - \frac{S}{n_i}u_i \\ -\frac{1}{m_i n_i}\frac{\partial (n_i k T_i)}{\partial x}, \tag{4}$$

where R_{ie} can be calculated using momentum conservation in ion-electron collisions. Charge exchange friction R_{CX} is given by

$$R_{CX} = -n_i m_i u_i |u_i| \sum_b n_b \sigma_{CX,b}, \tag{5}$$

where the sum is over neutral atomic states, and we simplify the expression by approximating the ions as cold, and the neutrals as cold and stationary. The constant charge exchange cross sections are approximated by the low energy values from Janev[15]

$$\sigma_{CX,1} = 3\times 10^{-19} m^2,$$
$$\sigma_{CX,2} = 2^4\times 10^{-19} m^2,$$
$$\sigma_{CX,3} = 3^4\times 7\times 10^{-20} m^2,$$
$$\sigma_{CX,b\geq 4} = b^4\times 6\times 10^{-20} m^2.$$

The electric field comes from Ampère-Maxwell's law

$$\frac{\partial E}{\partial t} = -\frac{1}{\epsilon_0}(j_e + Zen_i u_i), \tag{6}$$

where j_e is simply given directly by $j_e = -en_e u_e$.

Finally, the atomic state distribution of the neutrals must be tracked. This is done using a diffusive-reactive model

$$\frac{\partial n_b}{\partial t} = \frac{\partial}{\partial x}\left(D_b \frac{\partial n_b}{\partial x}\right) \\ + \sum_{b'<b}[K^e_{b'\to b} n_{b'} - A_{b\to b'} n_b - K^e_{b\to b'} n_b] \\ + \sum_{b'>b}[K^e_{b'\to b} n_{b'} + A_{b'\to b} n_{b'} - K^e_{b\to b'} n_b] \\ -K^{ion}_b n_b + \alpha_b n_e^2 n_i + \beta_b n_e n_i, \tag{7}$$

where we use moments of the electron distribution function (Maxwellian in fluid model) to calculate the ionization and (de)excitation rates K, as well as three-body recombination rates α. Neutrals are taken to be cold compared to the electrons for all rate calculations. The required atomic data are all taken from Janev[15] and NIST[16]. Data for spontaneous emission rates A is included up to state $b = 20$; however, this truncation should not introduce a substantial error for higher states, as those are primarily collisionally dominated. Finally, we include radiative recombination β as a function of temperature[15]. In order to include diffusion, we use the classical 1D diffusion coefficient

$$D_b = \frac{v_{tn}}{2[(n_i + n_1)\sigma_{el} + \sigma_{CX,b} n_i]} \tag{8}$$

for the sake of which we treat neutrals as having a thermal velocity v_{tn}, and assume that the diffusion is due to elastic collisions between ions and ground state neutrals and charge-exchange collisions with the ions. σ_{el} is the approximate elastic collisions cross-section $\sigma_{el} = \pi a_0^2$ (usually negligible compared to the charge-exchange contribution), and n_1 being the ground state density. The neutral temperature used to calculate v_{tn} is a free parameter (see Section 3).

At the sheath boundary, ions reach the sound speed (as per the Bohm criterion). In the fluid case, ambipolar flux is assumed, and the sheath heat transmission coefficient[17] in the transmitted sheath heat flux

$$q_{sh} = \gamma_e k T_e \Gamma_e, \tag{9}$$

is set to $\gamma_e = 5.5$. Neutrals are recycled with flux $\Gamma_{REC} = -R\Gamma_i$, where $R \leq 1$ and Γ_i is the ion flux to the target.

2.2. Electron kinetic equation

Starting from the classical 1D kinetic equation for the electrons

$$\frac{\partial f(x,\vec{v},t)}{\partial t} + v_x\frac{\partial f(x,\vec{v},t)}{\partial x} - \frac{e}{m_e}E\frac{\partial f(x,\vec{v},t)}{\partial v_x} = C[f,...], \tag{10}$$

where the RHS contains all of the collision and source operators, we expand the distribution function in spherical harmonics. We follow the approaches used in the codes KALOS[18] and OSHUN[19] and write the expansion as

$$f(v,\theta,\varphi) = \sum_{l=0}^{\infty}\sum_{m=-l}^{l} f_l^m(v) P_l^{|m|}(\cos\theta)\exp(im\varphi),$$
$$(f_l^m)^* = f_l^{-m}, \tag{11}$$

where θ is the angle between the velocity vector $\vec{v}$ and the x-axis, and $P_l^m(\cos\theta)$ are associated Legendre polynomials. Since the model is 1D and azimuthally symmetric, we set $m = 0$, and the expansion reduces to a Legendre polynomial expansion. Moments of scalar $\phi(v)$ and vector $\vec{a}(v)$ quantities are then simply

$$\int \phi f(\vec{v}) d\vec{v} = 4\pi \int_0^\infty \phi f_0(v) v^2 dv \tag{12}$$

$$\int a_x f(\vec{v}) d\vec{v} = \frac{4\pi}{3}\int_0^\infty ||a|| f_1 v^2 dv \tag{13}$$

with higher order tensors and 3D generalizations available in the literature[20, 19]. Thus we see that we can recover fluid quantities by taking appropriate moments of specific harmonics (e.g. f_0 for density, f_1 for flux, etc.).

The equations for each Legendre harmonic f_l have the form

$$\frac{\partial f_l(x,v,t)}{\partial t} = \mathcal{A}_l + \mathcal{E}_l + \mathcal{C}_l, \tag{14}$$

where $\mathcal{A}_l$ and $\mathcal{E}_l$ are the advection (Vlasov) terms, and $\mathcal{C}_l$ are all other operators. While the derivations (and some of the full forms) of these operators are beyond the scope of this paper, we give a brief overview below, and direct the reader to the literature where appropriate. The full details of the SOL-KiT model, as well as code numerics and benchmarking, will be the subject of a future publication[14]. However, for the sake of clarity of the presented results, we briefly discuss some numerical aspects of the code at the end of this section.

2.2.1. Vlasov terms The spatial advection term (advection in the x-direction), for a given harmonic l is

$$\mathcal{A}_l = -\frac{l}{2l-1} v \frac{\partial f_{l-1}}{\partial x} - \frac{l+1}{2l+3} v \frac{\partial f_{l+1}}{\partial x}, \tag{15}$$

while the velocity space advection[18] is given by

$$\mathcal{E}_l = \frac{e}{m} E \left(\frac{l}{2l-1} G_{l-1} + \frac{l+1}{2l+3} H_{l+1} \right), \tag{16}$$

$$G_l(v) = v^l \frac{\partial v^{-l} f_l}{\partial v}, \tag{17}$$

$$H_l(v) = \frac{1}{v^{l+1}} \frac{\partial v^{l+1} f_l}{\partial v}. \tag{18}$$

As can be seen from these equations, Vlasov terms couple different harmonics through either spatial gradients or the electric field.

2.2.2. Coulomb collision terms We consider the effect of Coulomb collisions on the distribution function f of particles with mass and charge m and $q = ze$, respectively, colliding with particles of mass and charge $M = \mu m$ and $Q = Ze$, which have a distribution F. Following the formalism of Shkarofsky et al.[20], we start with the Rosenbluth form of the Fokker-Planck collision operator

$$\frac{1}{\Gamma_{zZ}} \frac{\delta f}{\delta t} = \frac{4\pi}{\mu} F f + \frac{\mu - 1}{\mu + 1} \nabla \mathcal{H}(F) \cdot \nabla f + \frac{\nabla\nabla \mathcal{G}(F) : \nabla\nabla f}{2}, \tag{19}$$

where $\nabla = \partial/\partial \vec{v}$ and $\Gamma_{zZ} = (zZe^2)^2 \ln\Lambda / [4\pi(m_s \epsilon_0)^2]$. The Rosenbluth drag and diffusion coefficients are respectively $\mathcal{H}$ and $\mathcal{G}$. We linearize the collision operator in the anisotropic component of the distribution functions ($F = F_0 + F_a$, $f = f_0 + f_a$). After expanding the distribution function and the Rosenbluth coefficients in harmonics and using the integrals[20]

$$I_j(F_l) = \frac{4\pi}{v^j} \int_0^v F_l(u) u^{j+2} du, \tag{20}$$

$$J_j(F_l) = \frac{4\pi}{v^j} \int_v^\infty F_l(u) u^{j+2} du, \tag{21}$$

we get for $l = 0$

$$\frac{1}{\Gamma_{zZ}} \frac{\delta f_0}{\delta t} = \frac{1}{3v^2} \frac{\partial}{\partial v} \left[\frac{3}{\mu} f_0 I_0(F_0) + v \left(I_2(F_0) + J_{-1}(F_0) \right) \frac{\partial f_0}{\partial v} \right], \tag{22}$$

while for $l > 0$

$$\begin{aligned} \frac{1}{\Gamma_{zZ}} \frac{\partial f_l}{\partial t} &= \frac{4\pi}{\mu} \left[F_0 f_l + f_0 F_l \right] \\ &- \frac{(\mu - 1)}{\mu v^2} \times \\ &\left\{ \frac{\partial f_0}{\partial v} \left[\frac{l+1}{2l+1} I_l(F_l) - \frac{l}{2l+1} J_{-1-l}(F_l) \right] + I_0(F_0) \frac{\partial f_l}{\partial v} \right\} \\ &+ \frac{I_2(F_0) + J_{-1}(F_0)}{3v} \frac{\partial^2 f_l}{\partial v^2} \\ &+ \frac{-I_2(F_0) + 2J_{-1}(F_0) + 3I_0(F_0)}{3v^2} \frac{\partial f_l}{\partial v} \\ &- \frac{l(l+1)}{2} \times \frac{-I_2(F_0) + 2J_{-1}(F_0) + 3I_0(F_0)}{3v^3} f_l \\ &+ \frac{1}{2v} \frac{\partial^2 f_0}{\partial v^2} [C_1 I_{l+2}(F_l) \\ &+ C_1 J_{-1-l}(F_l) + C_2 I_l(F_l) + C_2 J_{1-l}(F_l)] \\ &+ \frac{1}{v^2} \frac{\partial f_0}{\partial v} [C_3 I_{l+2}(F_l) \\ &+ C_4 J_{-1-l}(F_l) + C_5 I_l(F_l) + C_6 J_{1-l}(F_l)], \end{aligned} \tag{23}$$

where the C coefficients are available in the literature[19]. For electron-electron collisions $\mu = 1$, and the collision operator for the isotropic part of the distribution function [21, 22] is

$$\frac{1}{\Gamma_{ee}} \left(\frac{\delta f_0}{\delta t} \right)_{e-e} = \frac{1}{v^2} \frac{\partial}{\partial v} \left[C(f_0) f_0 + D(f_0) \frac{\partial f_0}{\partial v} \right], \tag{24}$$

where the drag and diffusion coefficients are

$$C(f_0) = 4\pi \int_0^v f_0(u) u^2 du, \tag{25}$$

$$D(f_0) = 4\pi \int_0^v u^2 \left[\int_u^\infty f_0(u') u' du' \right] du. \tag{26}$$

The electron-electron collision operator for $l = 0$ is important for the proper relaxation of the electron distribution function to a Maxwellian. For the sake of brevity, we omit the electron-electron collision operator for higher harmonics (see [19, 20]), and note only that the $l = 1$ component redistributes momentum among the electrons.

As $T_e = T_i$, no $l = 0$ component for the electron-ion collision operator is used. For higher harmonics and stationary ions ($F_0 = n_i\delta(v)/(4\pi v^2)$) equation (23) reduces to the following eigenfunction form

$$\left(\frac{\delta f_l}{\delta t}\right)_{e-i} = -\frac{l(l+1)}{2}\frac{\Gamma_{ei}n_i}{v^3}f_l, \tag{27}$$

which is pitch-angle scattering. The eigenvalue is negative, so this operator dampens harmonics with high l. Thus one can truncate the expansion at some finite l. When ions are not stationary but their velocity is much smaller than the electron thermal velocity (the situation we expect in the SOL), we can approximate their distribution as a Dirac delta $F(\vec{v}) = n_i\delta(\vec{v} - \vec{u_i})$, which allows us to treat the plasma close to the divertor target.

2.2.3. Boltzmann collision terms To model electron-neutral collisions we use the Boltzmann collision integral for collisions between species s and s'

$$C[f_s, f_{s'}](v) = \int d\vec{v_2}d\Omega|\vec{v} - \vec{v_2}|\sigma(|\vec{v} - \vec{v_2}|, \Omega) \times$$
$$\times[f_s(\vec{v'})f_{s'}(\vec{v_2'}) - f_s(\vec{v})f_{s'}(\vec{v_2})], \tag{28}$$

where primed velocities denote values before a collision, and σ is the appropriate differential cross-section. Using a standard procedure for particle-conserving (e.g. excitation) inelastic collisions[20, 23, 24], we get

$$\left(\frac{\delta f_l}{\delta t}\right)^{ex}_{b\to b'} = -n_b v[\sigma^{TOT}_{b\to b'}(v)f_l(v)$$
$$-f_l(\alpha_p v)\alpha_p^2\left(\sigma^{TOT}_{b\to b'}(\alpha_p v) - \sigma^{(l)}_{b\to b'}(\alpha_p v)\right)], \tag{29}$$

where $\alpha_p = v'/v = (1 + 2\epsilon/mv^2)^{1/2}$, and σ^{TOT} is the integral cross section, while

$$\sigma^{(l)}(v) = \int d\Omega(1 - P_l(\cos\chi))\sigma(\chi, v),$$

where P_l are Legendre polynomials.

For ionization (and other collisions that do not conserve total number of particles), we take the simplest possible approach and add (or remove) electrons to (from) the lowest velocity cell[7], using

$$\left(\frac{\delta f_l}{\delta t}\right)^{ion}_{b} = \left(\frac{\delta f_l}{\delta t}\right)^{ex}(\sigma_b^{ion}) + n_b K_b^{ion}\frac{\delta(v)}{4\pi v^2}\delta_{l,0}, \tag{30}$$

where $\left(\frac{\delta f_l}{\delta t}\right)^{ex}(\sigma_b^{ion})$ is the particle conserving part, and $K_b^{ion} = 4\pi\int dvv^3 f_0(v)\sigma_b^{TOT,ion}(v)$.

For inverse processes we use the principle of detailed balance [25, 26] to obtain cross-sections. For deexcitation (from state i to j) this is

$$\sigma_{deex}(i, j, v') = \frac{g_j}{g_i}\frac{v^2}{v'^2}\sigma_{ex}(j, i, v), \tag{31}$$

where g_i and g_j are statistical weights (for hydrogen $g_n = 2n^2$). Velocities v' and v are related through the excitation energy. For 3-body recombination we use the statistical weights of a free electron gas to get

$$\sigma_{3b-recomb}(i, v')\frac{1}{n_e} = \frac{g_i}{2g_1^+}\left(\frac{h^2}{2\pi m_e kT_e}\right)^{3/2} \times$$
$$\times\frac{v^2}{v'^2}\sigma_{ion}(i, v), \tag{32}$$

where h is the Planck constant, and g_1^+ is the ion ground state statistical weight (for hydrogen $g_1^+ = 1$).

2.2.4. Electron heating operator The implemented diffusive heating operator has the form

$$\left(\frac{\partial f_0}{\partial t}\right)_{heating} = \Theta(L_h - x)D(x, t)\frac{1}{3v^2}\frac{\partial}{\partial v}v^2\frac{\partial f_0}{\partial v}, \tag{33}$$

where $\Theta(L_h - x)$ designates the heating region. If we assume a spatially uniform heating we get

$$D(t) = \frac{W_h(t)}{m_e\int_0^{L_h} n_e(x, t)dx}, \tag{34}$$

where $W_h(t)$ is the heat flux entering the SOL over length L_h. This is related to the fluid model heating Q as $Q = W_h/L_h$.

2.2.5. Divertor target boundary condition with Legendre polynomials Similarly to the fluid case, we set flow to be ambipolar at the sheath entrance. We then use the logical boundary condition[27], which assumes that all electrons with $v_x > v_c$ are lost, while all others are reflected. This translates to having a cut-off in the electron distribution function at $v_x = -v_c$. The challenge comes in decomposing this condition in Legendre polynomials. Fortunately, the number of required harmonics to capture the basic behaviour is usually not prohibitively high, with $l = 1$ enough for the condition to be satisfied, although higher harmonics will improve accuracy. We omit the derivation of the decomposition, and note that the "cut-off" distribution harmonics can be written as a linear combination of known harmonics

$$f_{cl}(v) = \sum_{l'} P_{ll'}f_{l'}(v), \tag{35}$$

where $P_{ll'}$ is the transformation matrix containing the details of the cut-off. With the distribution function form known, the ambipolarity condition is

$$\frac{4\pi}{3}\int_0^\infty v^3 f_{c1} dv = n_{i,sh}u_{i,sh}, \tag{36}$$

where $n_{i,sh}$ is the density at the sheath boundary, and $u_{i,sh}$ is the ion velocity at the boundary, given by the Bohm condition $u_i \geq c_s = [k(T_e+T_i)/m_i]^{1/2}$,where T_e is the electron temperature of the cut-off distribution, and T_i is the ion temperature. The ambipolarity condition gives v_c, and with it the sheath potential drop $\Delta\Phi = m_e v_c^2/(2e)$.

2.3. Model numerics

As previously noted, the details of the numerical methods used in SOL-KiT will be the topic of a future paper[14]. However, we present basic elements of the algorithm here to aid the presentation of results in the following sections.

SOL-KiT is a fully implicit 1D code. All operators are represented in matrix form, with nonlinear terms iterated to a desired accuracy. When switching between kinetic and fluid electrons, we simply restructure the model matrix to include elements calculated using the desired model. This does change the dimension of the matrix, as the kinetic model requires use of a velocity grid with number of cells N_v, as well as accommodating a number of harmonics up to l_{max}, whereas the fluid model needs only the staggered spatial grid with N_x cells.

Staggering of the spatial grid is simply perfomed by resolving the scalar (n_e,T_e,n_b,f_0, etc.) quantities in cell centres, while vector quantities (E,u_i,f_1, etc.) are given only on cell boundaries. For the simulations performed here, the spatial grid is logarithmic, with cells closer to the sheath boundary being smaller. This allows for better resolution close to the target, where spatial gradients are large. In all runs here $N_x = 64$.

The velocity grid used in the kinetic runs presented here is geometric, and velocity is normalised to $v_{th,0}$ - the electron thermal velocity for a reference temperature of 10 eV. This approach allows for properly capturing low energy electrons and their dynamics, as well as making sure the high energy tail is resolved. We use $N_v = 80$, with $l_{max} = 1$ (the diffusive approximation [28]), and take the smallest velocity grid cell width to be $dv = 0.05v_{th,0}$, while resolving velocities up to $\approx 12v_{th,0}$.

Finally, in order to capture the collisional dynamics during kinetic simulations of transients, we use a timestep that resolves the collision times in the system (see Section 4).

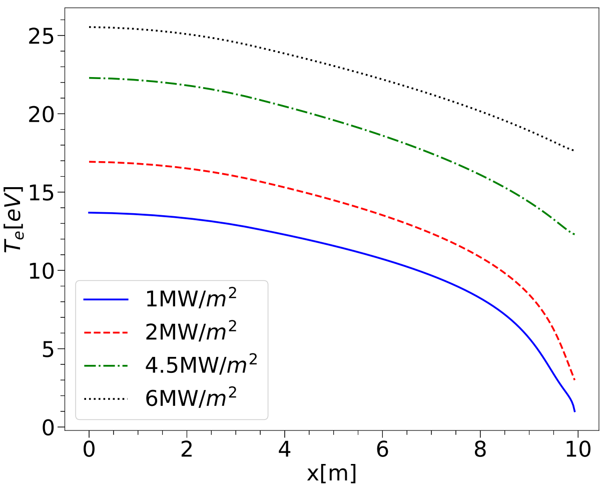

Figure 1. Equilibrium temperature profiles for a few representative powers from scan - electrons treated as a fluid.

3. Simulation setup and equilibrium results

We set up the simulations in the following way. The length of the domain is $L = 9.94\ m$, with the heat source injecting energy over $L_h = 3.51\ m$ upstream. The total (plasma and neutral) line-averaged density is kept at $\langle n_{tot}\rangle_L = 1\times10^{19}\ m^{-3}$ by utilizing 100% recyling ($R = 1$). Recycling produces deuterium atoms with temperature $T_n = 3$ eV (mimicking Franck-Condon enhancement [17]), and we track a total of 30 atomic states.

The first set of simulations we describe is an input power scan using fluid electrons. Note that all equilibrium results presented here were obtained by running the code until there were no significant transients remaining (as such, the initial condition influences only the time required to reach equilibrium). The effective input power flux was varied from $1MW/m^2$ to $6MW/m^2$. The input power range used allows us to consider qualitatively different regimes, while staying in a parameter range relevant to MSTs. Figure 1 shows temperature profiles from several of the fluid electron runs. As expected, the temperature profile starts flattening as input power is increased.

Figure 2 shows the density profile behaviour for these runs. As the power increases, the density peak grows and moves closer to the divertor target. However, after the neutrals have been forced sufficiently close to the boundary, the plasma density profile starts flattening. The ground state neutral density is shown in Figure 3, where we see the neutrals being depleted with increasing power.

Temperature profiles for runs with kinetic electrons are presented in Figure 4. We can see that the temperature profiles are steeper, with higher temper-

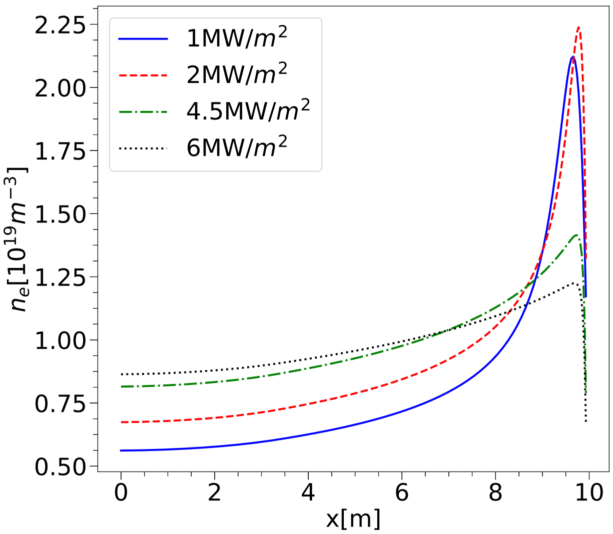

Figure 2. Density profiles for runs from Figure 1 - the density peak grows and moves towards the target, until the profile begins flattening.

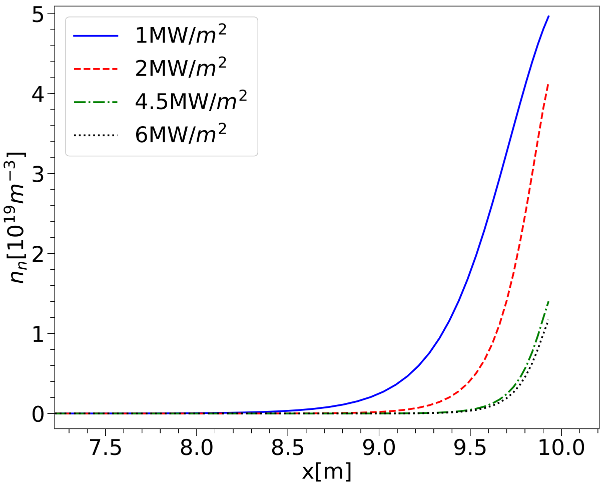

Figure 3. Ground state neutral density profiles for runs from Figure 1 - as input power grows the neutral population diminishes.

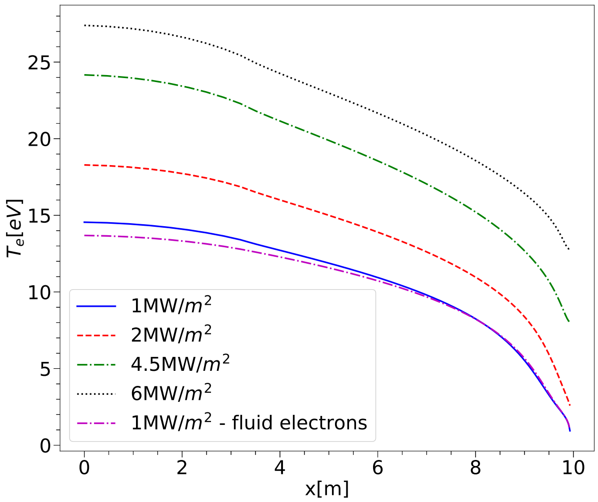

Figure 4. Equilibrium temperature profiles when electrons are treated kinetically; the profile is steeper, with upstream temperatures greater than in the fluid case, as can be seen from the included fluid equilibrium (purple dash-dotted line).

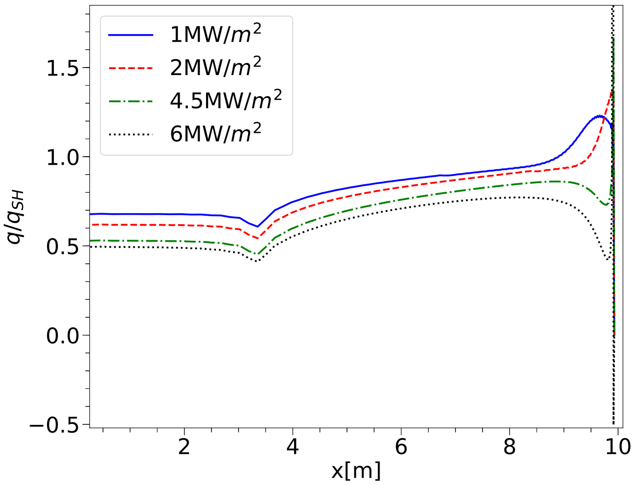

Figure 5. Ratio of calculated conductive heat flux to the classical local value. Upstream heat flux is suppressed, while lower input power runs show flux enhancement near the boundary. Negative values of the ratio are due to the temperature uptick - most likely a consequence of the $T_i = T_e$ approximation.

atures at the upstream and lower downstream, compared to the fluid electron case. The isotropic diffusive heating operator produces a small imprint in the temperature profile, evident from the change in slope around $x = 3.5\ m$ (however, the effective heating power is the same as in the fluid runs). A minor uptick (change in gradient sign) in the electron temperature at the target is present for higher power runs. While not visible in Figure 4 due to being localised close to the target, the effects of the uptick are visible in other quantities (see below, Figure 5). We expect this to be the consequence of taking $T_i = T_e$, as the lower collisionality should decouple electron and ion temperatures, leading to different pressure and electric field profiles, and this is not captured in our model.

The increased steepness of temperature profiles in simulations with kinetic electrons can be readily explained by looking at the ratio of the calculated conductive heat flux q to the classical Spitzer-Härm value based on the local temperature profile q_{SH}. This is shown in Figure 5, where we see that the heat flux upstream is suppressed (we also see again the imprint of the heating operator). Near the target the heat flux is enhanced for the lower heating powers, and the slight temperature uptick at the boundary causes the ratio to go negative, since the calculated Spitzer-Harm heat flux changes sign. These results are qualitatively similar to those obtained by Batishchev et al. [7] using a code where all species were treated kinetically, with the discrepencies seemingly due primarily to the use of an isotropic heating operator and the $T_i = T_e$ approximation.

Density profile behaviour during kinetic runs is qualitatively similar to that during simulations with fluid electrons, and we omit plots for the sake of brevity.

In order to further illustrate the differences between the kinetic and fluid model, we write here a simple Two-Point Model (2PM) [17] result for the temperature where an input heating flux q_{in} is distributed along a heating length L_h

$$T_u = \left[T_d^{7/2} + \frac{7}{2}\frac{q_{in}(L - L_h/2)}{\kappa_e}\right]^{2/7}. \quad (37)$$

We plot $T_u^{7/2} - T_d^{7/2}$ as a function of input power in Figure 6 for both the obtained fluid and kinetic equilibria, as well as the above 2PM. The fluid results appear to agree well with the 2PM, although the densities (similar to those in Figure 2) do not obey the predictions of the model. This is due to the presence of sources and sinks, and the resulting change in pressure balance. The kinetic simulations show a systematic increase of the calculated difference, which points to a reduction in the effective conductivity $\kappa_{e,eff} < \kappa_e$ in the above model. This is the consequence of flux suppression. However, note that the details of the flux suppression or enhancement depend on the input power and location within the system. As such, there appears to be no simple way (e.g. flux limiters) to capture the entirety of the kinetic effects.

Figure 7 shows the $l = 0$ harmonic in the last cell before the boundary for the 1MW/m^2 input power kinetic background. Comparing it to a Maxwellian distribution of equivalent density and temperature reveals a "hot" tail of electrons, which modify the transport properties as seen above.

Finally, we present results for the particle and energy fluxes into the target sheath. Figure 8 shows the variation of the particle flux into the sheath with input power. At 4.5MW/m^2 we observe the start of a flux rollover in the kinetic electron simulations. The fluid case is different, as rollover happens around 3MW/m^2. A slight increase in particle flux for higher powers is observed in the fluid case, and this can be explained by the increase of plasma density due to increased ionization (while the total line averaged density is kept constant). We interpret the particle rollover as the onset of detachment, and restrict equilibria to input powers below 4.5MW/m^2 (i.e. detached at least in the kinetic case) in the following section.

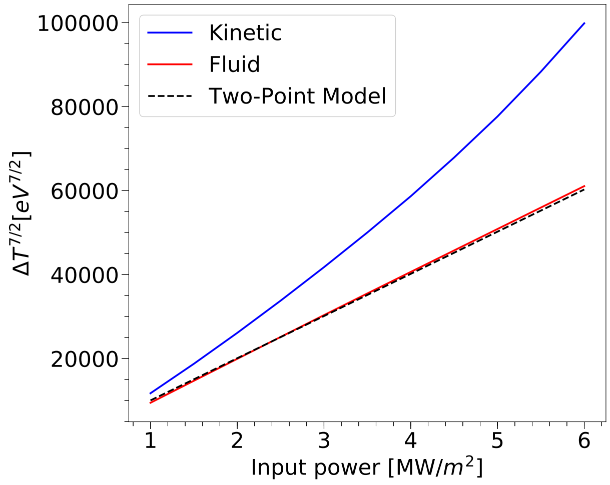

Figure 6. $T_u^{7/2} - T_d^{7/2}$ as a function of input power for the obtained equilibria. The Two-Point Model result is given as the dashed line, and appears to agree well with the fluid simulation results. Kinetic simulations show a systematically increased gap, further illustrating the effect of flux suppression.

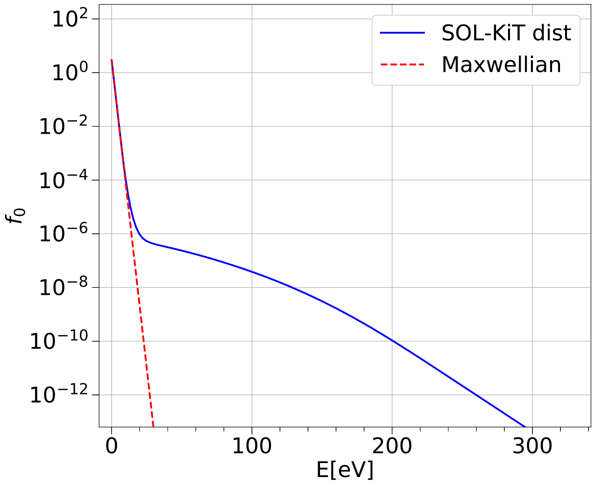

Figure 7. The $l = 0$ harmonic near the target sheath for the kinetic 1MW/m^2 input power run. The dashed line shows a Maxwellian with equivalent density and temperature. Fast electrons start appearing in the distribution from $\approx 15eV$.

We plot the value of the sheath heat transmission coefficient (see 9) as a function of input power in kinetic runs in Figure 9. Note that for the fluid runs it is set to $\gamma_e = 5.5$. Around 3.5MW/m^2 the coefficient experiences a rollover-like effect. This behaviour can

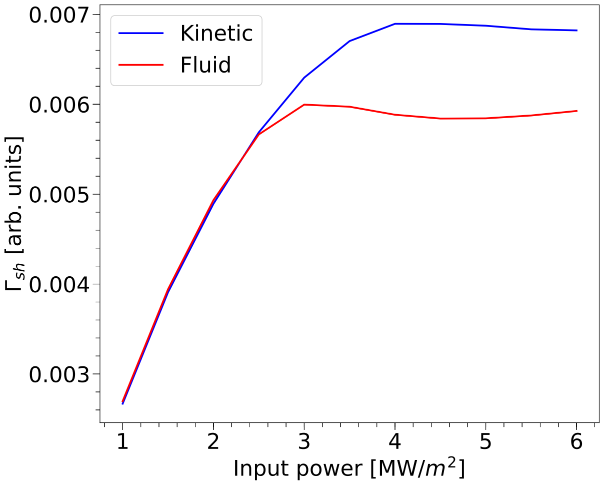

Figure 8. The particle flux into the target sheath as a function of input power. We observe rollover starting at 4.5MW/m^2, indicating onset of detachment below this input power.

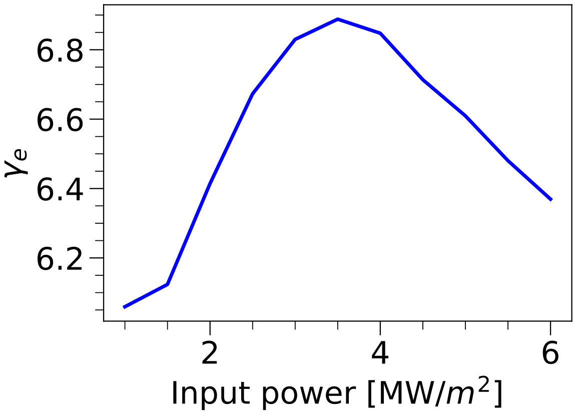

Figure 9. The electron sheath heat transmission coefficient as a function of input power when electrons treated kinetically. Rollover-like behaviour observed around 3.5MW/m^2.

be explained as follows. In the low input power limit we expect collisions to dominate and the regime to be well described with a fluid model, thus setting γ_e to its classical value. The high input power limit should produce a flat temperature profile, and with no gradients we again expect to return to the local value of ≈ 5.5. Thus if there is any change in γ_e we expect rollover-like behaviour at an intermediate input power. An explanation of why the heat transmission coefficient increases could be the same as for flux enhancement, i.e. the presence of hot electrons in the tail of an otherwise cold electron distribution.

Table 1. Possible combinations of equilibria and perturbations based on equilibrium and perturbation physics used.

	Fluid perturbation	Kinetic perturbation
Kinetic equilibrium	NA	kinetic on kinetic
Fluid equilibrium	fluid on fluid	kinetic on fluid

4. Transient simulations

Transient simulations were performed by starting from the above equilibria, and increasing the input power flux to 45MW/m^2 for $\approx 10\mu s$. After this the input power was returned to its original value for a further $\approx 10\mu s$, allowing the perturbation to relax. We use only equilibria with input powers up to 4.5MW/m^2, as we (somewhat conservatively) treat the plasma as attached for powers higher than this. In order to resolve collisions properly, we set the timestep in these simulations to ≈ 3 ns. Since SOL-KiT allows moving from fluid to kinetic simulations, it is possible to launch a kinetic perturbation on a fluid background. This would significantly reduce run time, as fluid equilibria converge much faster. We explore this below, considering the three possible combinations of equilibria and perturbation physics, as presented in Table 1.

Figure 10 shows the evolution of the perturbation on the 1MW/m^2 input power background for the various combinations in Table 1. The two kinetic models (kinetic perturbation on kinetic/fluid background) agree qualitatively, while the fluid model greatly overestimates heat flow, and consequently the temperature at the target.

The evolution of temperature at the target sheath boundary for several background input powers is shown in Figure 11, for the fluid and fully kinetic case, respectively. As can be seen, the peak temperatures at the target in the kinetic case are up to almost two times lower than in the fluid case. However, the temperature decays faster in the fluid than in the kinetic model, which is most likely due to the suppressed upstream flux relaxing more slowly.

It is useful to observe the evolution of the q/q_{SH} ratio during the perturbation. We focus on two locations, one in the middle of the domain, and one close to the target. These results are shown in Figures 12 and 13. The midpoint ratio evolution indicates an initial bout of flux enhancement (compared to the equilibrium), after which the heat flux is heavily suppressed. We note here that the lowest power equilibrium has the strongest kinetic response to the perturbation, which is also visible in Figure 13, where it experiences much greater enhancement compared to other equilibria. We expect this to be due to lower power equilibria having a much larger energy contrast between the local cold and the much hotter electrons

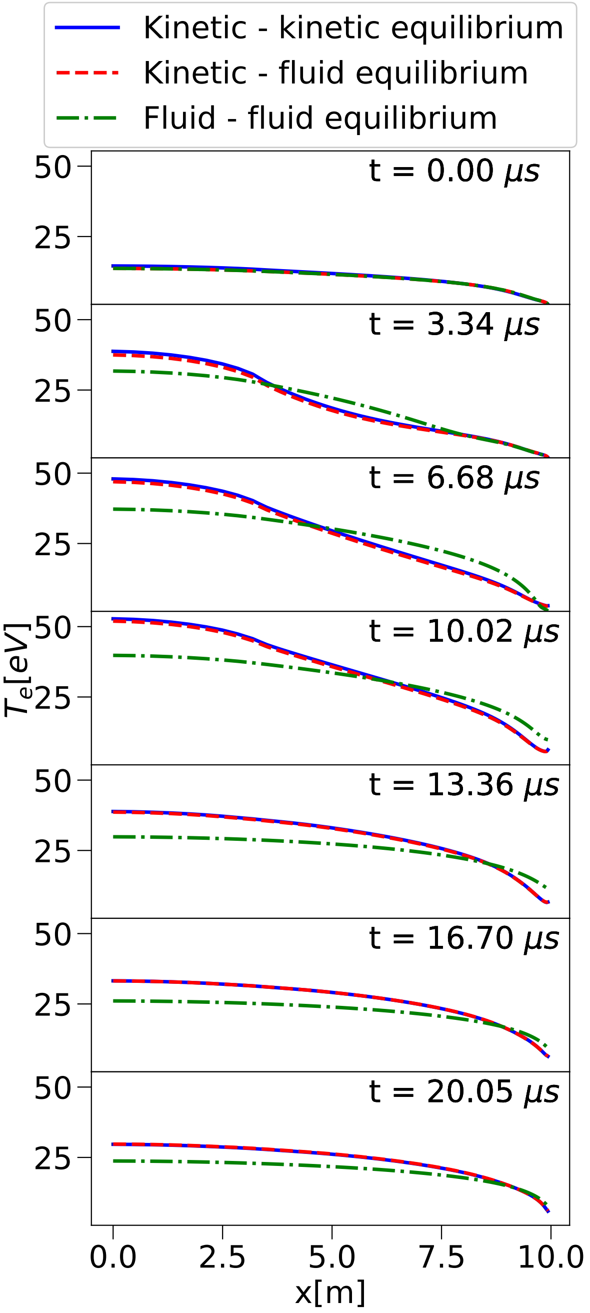

Figure 10. Temperature profile evolution for perturbation launched on the $1\mathrm{MW}/m^2$ background. The fluid model greatly overestimates the target temperature, while the two kinetic simulations have a similar qualitative behaviour, with a significantly higher upstream temperature than the fluid model during the perturbation.

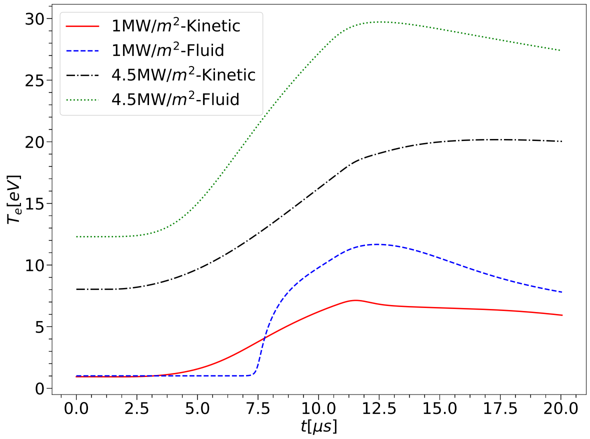

Figure 11. Evolution of the temperature perturbation at the target for the highest and lowest input powers considered. Presented are both a fluid perturbation and a kinetic perturbation on kinetic background.

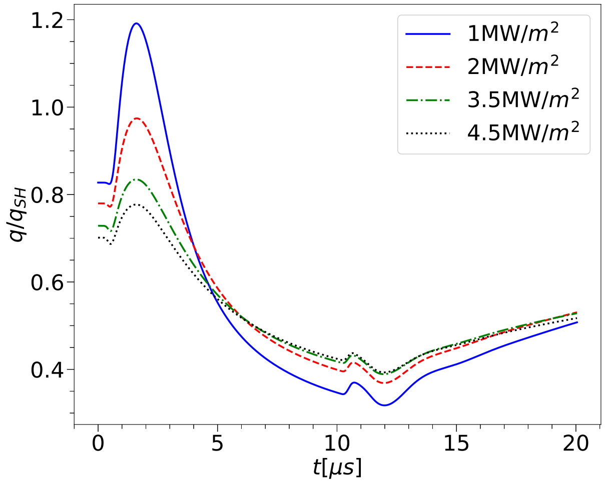

Figure 12. Ratio of calculated conductive heat flux to the local value during the kinetic perturbation run. Shown are several different background input powers at $x = 5\ m$. After an initial period of enhancement, the flux is heavily suppressed.

coming from upstream (see Figure 14 below).

The evolution of the $l = 0$ harmonic in the last cell before the boundary is presented in Figure 14, corresponding to the solid line in the first four subfigures of Figure 10, with the perturbation being launched on the $1\mathrm{MW}/m^2$ input power kinetic background. As expected, the perturbation manifests itself as a growing tail of energetic electrons.

We now turn to the evolution of the sheath properties, namely the sheath heat transmission coefficient and the sheath potential drop. Presented in Figures 15 and 16 is the heat transmission coefficient during the perturbation for several input powers, with

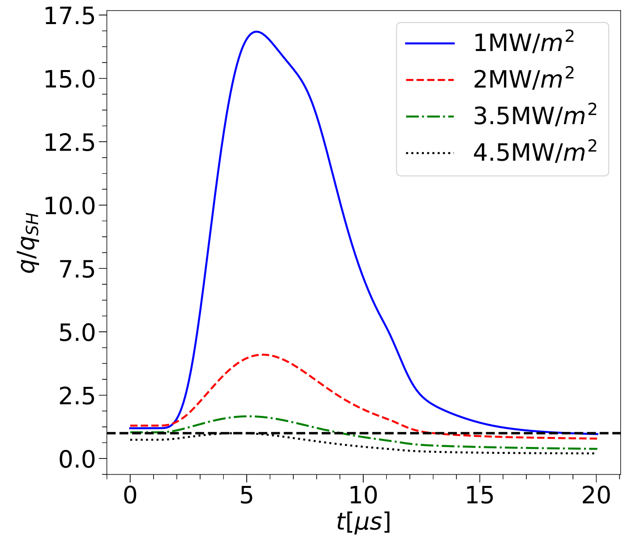

Figure 13. Ratio of calculated conductive heat flux to the local value during the kinetic perturbation run. Shown are several different background input powers at $x = 9.84\ m$. Close to the target, heat flux enhancement dominates during most of the perturbation. Dashed horizontal line shows $q/q_{SH} = 1$ for reference.

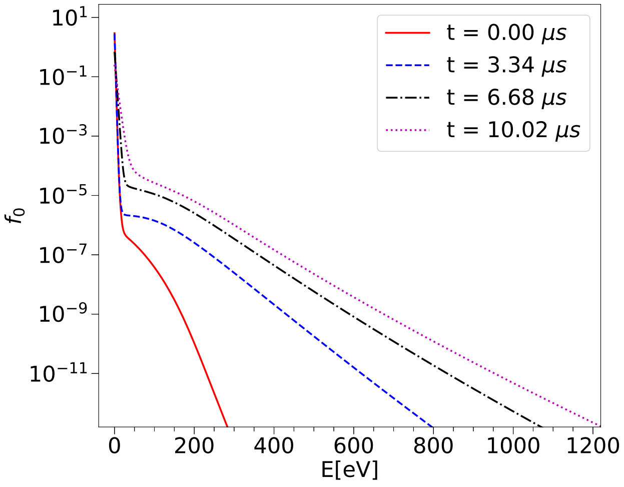

Figure 14. Evolution of the $l = 0$ harmonic near the boundary during the perturbation on the $1\text{MW}/m^2$ input power background (kinetic on kinetic background). This corresponds to the solid line in the first four subfigures of Figure 10.

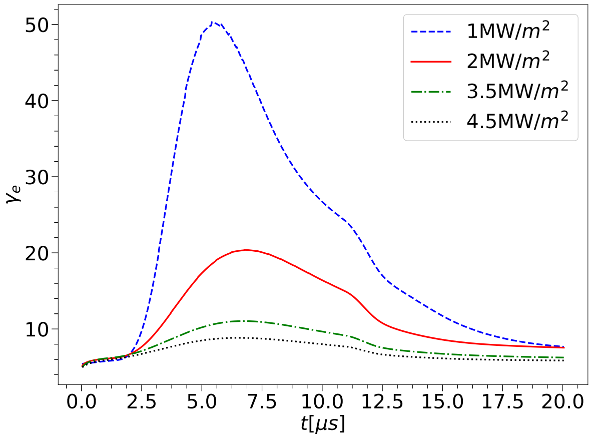

Figure 15. The sheath heat transmission coefficient during perturbations launched on several different initial input power backgrounds - kinetic perturbation on fluid background.

the kinetic perturbation launched on the fluid and kinetic backgrounds, respectively. Firstly, we observe that the sheath heat transmission coefficient can vary significantly during the perturbation, up to almost a factor of 10 for the strongest variation. Furthermore, the same sensitivity of lower initial power runs to kinetic effects observed in Figures 12 and 13 is seen here as well, with the $1\text{MW}/m^2$ background experiencing the largest variation in the value of γ_e. Finally, we note the differences between Figures 15 and 16, the first being the underestimation of γ_e when the perturbation is launched on a fluid background. This "error" grows as we reduce the initial input power, even though the qualitative behaviour is captured. Secondly, as can be seen from the first $\approx 2\mu s$ of the simulation, the fluid background experiences transients unrelated to the perturbation, but caused by switching to the kinetic model. While the background is relaxing in this way, the inherent transients become superimposed onto the incoming perturbation, making detailed interpretation of results difficult.

Similarly to the sheath heat transmission coeficient, the potential drop (normalized to kT_e/e) experiences variation during the perturbation. This is shown in Figures 17 and 18, for kinetic perturbations launched on fluid and kinetic backgrounds, respectively. We see that the potential varies up to around a factor of 2 (compared to the classical result of ≈ 3.0), and that the lowest initial power runs are again the most susceptible to the variation. While the peak value difference between simulations performed with fluid and kinetic backgrounds is less than that of the sheath heat transmission coefficient, there is still a considerable amount of discrepancy at the start of the simulations, most likely caused by the same relaxation transients men-

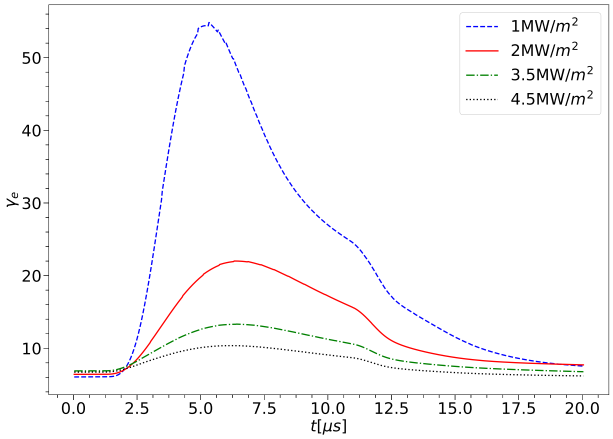

Figure 16. The sheath heat transmission coefficient during perturbations launched on several different initial input power backgrounds - kinetic perturbation on kinetic background.

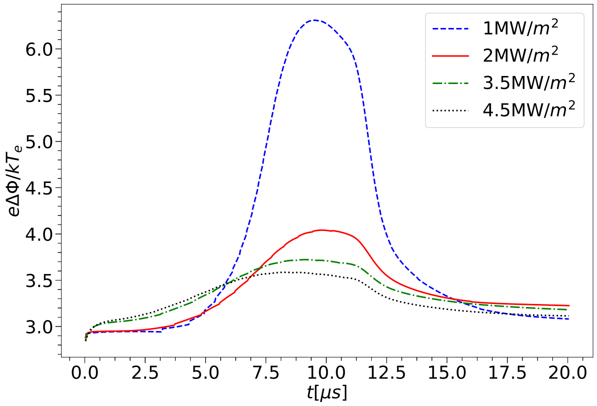

Figure 17. The sheath potential drop during perturbations launched on several different initial input power backgrounds - kinetic perturbation on fluid background.

tioned. Finally, we note that the jagged lines in Figures 15-18 are a finite velocity grid effect, due to the calculation of the cut-off velocity for the logical sheath boundary condition (see 36), which involves interpolation on the velocity grid.

5. Discussion

We begin the discussion of the presented results by going over the main limitations of the present study inherent to the model used, as well as limitations of scope. The first major assumption is that of dimensionality, as we use a 1D model. However, for the study of kinetic effects in the SOL, especially as they relate to equivalent fluid scenarios, we expect this study to be able to capture the fundamental differences.

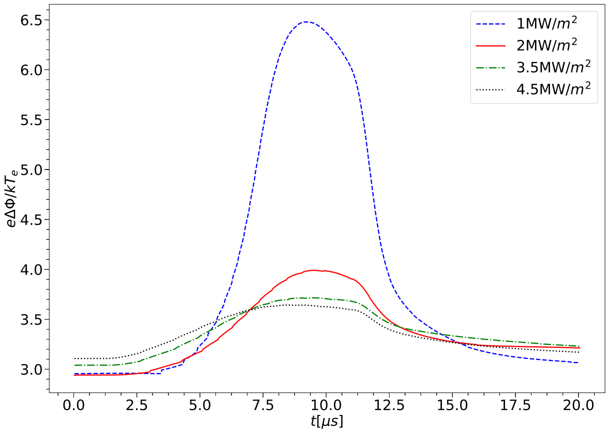

Figure 18. The sheath potential drop during perturbations launched on several different initial input power backgrounds - kinetic perturbation on kinetic background.

Two limitations we plan to tackle in a future version of the SOL-KiT code are the $T_i = T_e$ approximation, as well as the limited neutral physics (currently only diffusive-reactive atoms included, with elastic electron-neutral collisions ignored). These two primarily limit the parameter space accessible to us, and the fundamental aspects of the results presented in this study should not be greatly affected by them, especially since the study is based on comparing two models which use the same approximations. However, future work is being planned to investigate this rigorously.

Use of harmonics only up to $l = 1$ is another simplification in the current study. While this approximation captures most of the physics, simulations using it will naturally underresolve kinetic effects, as the allowed anisotropy of the distribution function is limited. Furthermore, we expect the greatest impact of including higher l terms to be at the boundary, where a better angular resolution in velocity space allows for higher accuracy in the sheath boundary condition. Exploring higher harmonic effects will be the topic of a future study, as SOL-KiT has all of the necessary features, with the only constraint being the computational time required to obtain kinetic equilibria with a high level of anisotropy. Preliminary results with higher harmonics confirm that they tend to be localized near the boundary.

We have presented in this study both equilibrium and transient simulations of parallel electron transport in the SOL, treating the electrons as either a fluid or kinetically. The equilibrium results (for the parameters in this study), while showing the presence of kinetic effects, do not appear to be dominated by them. We report the rollover of the plasma flux into the target sheath, which is interpreted as the onset of detachment.

The input power at which this occurs is different for the fluid and kinetic models, with the rollover happening at a lower input power when electrons are treated as a fluid. Rollover at a lower power in the fluid case can be explained by the fact that temperatures near the target are greater compared to the kinetic model, leading to a higher degree of ionization. The equilibrum kinetic effects, which occur as heat flux enhancement and suppression, depend heavily on the spatial location and the input power. This makes it difficult to prescribe one (or even a set) of flux limiters that could capture the physics, especially the flux enhancement. Another equilibrium kinetic effect that has been explored here is the modification of the electron sheath heat transmission coefficient, where we find up to $\approx 20\%$ variation with respect to the assumed classical fluid value of $\gamma_e = 5.5$.

While a clear dominance of kinetic effects was not found for the equilibrium simulations, runs with transients provide a different picture. Firstly, the target temperature during the perturbation predicted by the fluid model is considerably higher than when electrons are treated kinetically (Figure 11). One could imagine imposing a flux limiter in the fluid case to mimic this, but we present results showing vastly different evolution of the conductive electron heat flux (with respect to its classical value) for both different spatial points in the system, as well as different initial input powers (see Figures 12 and 13). With a mix of heat flux suppression and enhancement, as well as their time-dependant nature, it is highly unlikely that a simple modification to the flux could reproduce the full range of behaviours simulated here. However, it might be worthwhile to explore more complicated fluid models for capturing kinetic effects (see, for example, Brodrick et al.[29]), and compare them to the results obtained in this study. We also present the variation of the sheath heat transmission coefficient, as well as the sheath potential drop, during the perturbation. Both show significant modification compared to their classical values, indicating a likely need to include time-dependant models for the sheath behaviour during transients simulated using fluid codes.

It is worth repeating that all of the presented perturbation simulations were performed in the same way, increasing the input power to the same value ($45\text{MW}/m^2$) for the same amount of time (approximately $10\mu s$). However, the intensity of kinetic effects varied strongly as a function of initial conditions, namely the initial input power of the used equilibrum profiles. This suggests, as one might expect, that the degree of kinetic modification to the physics depends on the ratio of the initial input power to that of perturbation. Further investigation is required to explore this facet of the simulations, with a special focus on the way energy is injected into the system.

Finally, we explored the approach of launching kinetic perturbations on fluid equilibria. While there are discrepancies due to the fluid equilibrium relaxing (see for example Figures 15 and 16), the perturbation behaviour is well captured using this approximate method. As the equilibria are reached on fluid timescales, the fact that the kinetic model requires a much shorter timestep increases simulation times. In some cases an increase of more than 30 times was required to reach equilibrium (computational requirements to be presented in dedicated code paper[14]). Since the computational time saved when using a fluid equilibrium as the base for kinetic transient studies is considerable, having the option of performing quick simulations to explore qualitative aspects of the perturbation behaviour is encouraging.

The parameter ranges of the presented results are mostly relevant to MSTs, specifically to the interaction of transients with detachment in such machines. In larger machines, we expect that for similar collisionalities to those treated here the kinetic effects would manifest in a qualitatively similar manner. This would require a corresponding scaling up of the input power and density in order to compensate for an increase in connection length. As our simulations require resolving the collision times, denser plasmas would be much more computationally expensive.

6. Conclusion

We presented the first study of parallel electron transport using the newly developed fully implicit code SOL-KiT. Both equilibria and transients were simulated, using the capability of the code to self-consistently simulate electrons as a fluid or kinetically. The parameters used in these simulations are mostly relevant to medium sized tokamaks.

Significant kinetic effects were found during transients, especially in the transport properties of the target sheath, where it was found that the electron sheath heat transmission coefficient could reach almost 10 times its classical value. We compare simulations using different initial conditions as well as different models for the electrons (fluid or kinetic), and find both heat flux suppression and enhancement in both equilibrium and transient simulations. The fluid model is found to systematically overestimate the temperature at the target due to a lack of heat flux suppression. A considerable amount of sensitivity to initial conditions was observed in transient simulations, with different backgrounds experiencing greatly varying levels of kinetic effects.

We show that an accurate prediction of the evolution of heat flux during transients in the SOL requires a kinetic approach to modeling electrons, as the variable transport quantities during transients would be extremely difficult to simulate using flux limiters.

Acknowledgements

This work was supported through the Imperial President's PhD Scholarship scheme. This work was partially funded by the RCUK Energy Programme [grant number: EP/P012450/1]. Simulation results were obtained with the use of the Imperial College Research Computing Service [30]

References

[1] A. Loarte, B. Lipschultz, A. S. Kukushkin, G. F. Matthews, P. C. Stangeby, N. Asakura, G. F. Counsell, G. Federici, A. Kallenbach, K. Krieger, A. Mahdavi, V. Philipps, D. Reiter, J. Roth, J. Strachan, D. Whyte, R. Doerner, T. Eich, W. Fundamenski, A. Herrmann, M. Fenstermacher, P. Ghendrih, M. Groth, A. Kirschner, S. Konoshima, B. Labombard, P. Lang, A. W. Leonard, P. Monier-Garbet, R. Neu, H. Pacher, B. Pegourie, R. A. Pitts, S. Takamura, J. Terry, and E. Tsitrone. Chapter 4: Power and particle control. *Nuclear Fusion*, 47(6), 2007.

[2] S. I. Braginskii. Transport processes in a plasma. *Reviews of Plasma Physics*, 1:205–311, 1965.

[3] W. Fundamenski. Parallel heat flux limits in the tokamak scrape-off layer. *Plasma Physics and Controlled Fusion*, 47(11):R163–R208, 2005.

[4] A. V. Chankin and D. P. Coster. Comparison of 2D models for the plasma edge with experimental measurements and assessment of deficiencies. *Journal of Nuclear Materials*, 390-391(1):319–324, 2009.

[5] D. Tskhakaya, F. Subba, X. Bonnin, D. P. Coster, W. Fundamenski, and R. A. Pitts. On kinetic effects during parallel transport in the SOL. *Contributions to Plasma Physics*, 48(1-3):89–93, 2008.

[6] D. Tskhakaya. On Recent Massively Parallelized PIC Simulations of the SOL. *Contributions to Plasma Physics*, 52(5-6):490–499, 2012.

[7] O. Batishchev, M. M. Shoucri, A. A. Batishcheva, and I.P. Shkarofsky. Fully kinetic simulation of coupled plasma and neutral particles in scrape-off layer plasmas of fusion devices. *Journal of Plasma Physics*, 61(2):347–364, 1999.

[8] Z. AbouAssaleh, M. Petravic, R. Vesey, J. P. Matte, and T. W. Johnston. NonLocal Transport in a Tokamak Plasma Divertor with Recycling. *Contributions to Plasma Physics*, 34(2-3):175–179, 1994.

[9] F. Allais, J. P. Matte, F. Alouani-Bibi, C. G. Kim, D. P. Stotler, and T. D. Rognlien. Modification of atomic physics rates due to nonlocal electron parallel heat transport in divertor plasmas. *Journal of Nuclear Materials*, 337-339(1-3 SPEC. ISS.):246–250, 2005.

[10] A.V. Chankin and D.P. Coster. On the locality of parallel transport of heat carrying electrons in the SOL. *Journal of Nuclear Materials*, 463:498–501, 2015.

[11] M. Zhao, A. V. Chankin, and D. P. Coster. Kinetic simulations of electron heat flux in the scrape-off layer. *Nuclear Materials and Energy*, 12:819–824, 2017.

[12] A. V. Chankin, G. Corrigan, and A. E. Jaervinen. Assessment of the strength of kinetic effects of parallel electron transport in the SOL and divertor of JET high radiative H-mode plasmas using EDGE2D-EIRENE and KIPP codes. *Plasma Physics and Controlled Fusion*, 60, 2018.

[13] E. Havlíčková, W. Fundamenski, D. Tskhakaya, G. Manfredi, and D. Moulton. Comparison of fluid and kinetic models of target energy fluxes during edge localized modes. *Plasma Physics and Controlled Fusion*, 54(4), 2012.

[14] S. Mijin et al. SOL-KiT - fully implicit code for kinetic simulation of parallel electron transport in the tokamak Scrape-Off Layer. *- In preparation*, 2019.

[15] R. K. Janev, D. Reiter, and U. Samm. Collision Processes in Low-Temperature Hydrogen Plasmas. *Sciences-New York*, page 190, 2003.

[16] A. Kramida, Yu. Ralchenko, J. Reader, and NIST ASD Team (2018). Nist atomic spectra database. `https://physics.nist.gov/asd`. Accessed: 8th Dec 2017.

[17] P. Stangeby. *The Plasma Boundary of Magnetic Fusion Devices*, volume 43. 2000.

[18] A. P. L. Bell, A. R. Robinson, M. Sherlock, R. J. Kingham, and W. Rozmus. *Plasma Phys. Control. Fusion*, 48, 2006.

[19] M. Tzoufras, A. R. Bell, P. A. Norreys, and F. S. Tsung. A Vlasov-Fokker-Planck code for high energy density physics. *Journal of Computational Physics*, 230(17):6475–6494, 2011.

[20] I. P. Shkarofsky, T. W. Johnston, and Bachynski M. P. Addison Wesley, 1966.

[21] E. M. Epperlein. Implicit and Conservative Diference Scheme for the Fokker-Planck Equation, 1994.

[22] R. J. Kingham and A. R. Bell. An implicit Vlasov-Fokker-Planck code to model non-local electron transport in 2-D with magnetic fields. *Journal of Computational Physics*, 194(1):1–34, 2004.

[23] T. Makabe and Z. Petrovic. *Plasma Electronics*. 2nd edition.

[24] K. Kumar, H. R. Skullerud, and R. E. Robson. Kinetic Theory of Charged Particle Swarms in Neutral Gases. *Australian Journal of Physics*, 33(2):343, 1980.

[25] A. Bogaerts, R. Gijbels, and J. Vlcek. Collisional-radiative model for an argon glow discharge. *Journal of Applied Physics*, 84(1):121–136, 1998.

[26] G. Colonna, L. D. Pietanza, and M. Capitelli. Coupled solution of a time-dependent collisional-radiative model and Boltzmann equation for atomic hydrogen plasmas: Possible implications with LIBS plasmas. *Spectrochimica Acta - Part B Atomic Spectroscopy*, 56(6):587–598, 2001.

[27] R. J. Procassini, C. K. Birdsall, and B. I. Cohen. Particle simulations of collisional transport in a high recycling, diverted tokamak scrape-off layer. *Nuclear Fusion*, 30(11):2329–2348, 1990.

[28] E. M. Epperlein, G. J. Rickard, and A. R. Bell. A code for the solution of the Vlasov-Fokker-Planck equation in 1-D or 2-D. *Computer Physics Communications*, 52(1):7–13, 1988.

[29] J. P. Brodrick, R. J. Kingham, M. M. Marinak, M. V. Patel, A. V. Chankin, J. T. Omotani, D. Umansky, M. V.and Del Sorbo, B. Dudson, J. T. Parker, G. D. Kerbel, M. Sherlock, and C. P. Ridgers. Testing nonlocal models of electron thermal conduction for magnetic and inertial confinement fusion applications. *Physics of Plasmas*, 24(9):092309, 2017.

[30] Imperial College Research Computing Service, https://doi.org/10.14469/hpc/2232.